

Research Article

Particle Flow Analysis of Macroscopic and Mesoscopic Failure Process of Salt Rock under High Temperature and Triaxial Stress

Haoran Li,¹ Ziheng Wang,¹ Dekang Li ^{1,2} and Yajun Zhang¹

¹Shijiazhuang Tiedao University, Shijiazhuang, Hebei, China

²Institute of Geophysics, China Earthquake Administration, Beijing, China

Correspondence should be addressed to Dekang Li; dekanqli@163.com

Received 3 August 2021; Revised 2 October 2021; Accepted 15 October 2021; Published 15 November 2021

Academic Editor: Yu Wang

Copyright © 2021 Haoran Li et al. This is an open access article distributed under the Creative Commons Attribution License, which permits unrestricted use, distribution, and reproduction in any medium, provided the original work is properly cited.

In order to reveal the mechanism of thermal-induced deformation and fracture development of salt rock under high temperature, the particle flow program PFC^{2D} was used to study the triaxial compression failure process of salt rocks under different temperatures; at the same time, a combination model of Burge and Linearbond was proposed to simulate plastic deformation and heat conduction of salt rock. Finally, the simulation results were compared with the experimental results to verify the validity of the conclusion. The simulation results show that the elastic limit points of rock gradually descend, the dilatancy points rise gradually, and the plastic deformation characteristics of salt rock become more obvious with the increase of temperature. Due to the damage of the sample, the strong chains break and disappear, increasing the proportion of the weak chains, and the high temperature intensifies the rupture of the contact between the particles in the salt rock. As the temperature increases from 50°C to 120°C, the strong chains in the rock sample decrease significantly, and the damage gradually increases; when the temperature is 150°C, the contact force decreases sharply, and the damage of salt rock is significant. According to the particle displacement cloud diagrams, it is found that the expansion direction from the middle part of the rock sample to the left and right ends is 12.08°, 9.55°, 8.2°, 6.33°, and 0°, respectively. The displacement directions of the rock sample show obvious radial expansion tendency, and the higher the temperature, the more obvious the “drum-shaped” failure phenomenon in the middle of the rock sample. During the heating process, the thermal cracks are mainly tensile cracks, and transverse cracks are gradually formed in the middle of the model. The cementation failure points at the top and bottom of the model expand in an oblique direction and form oblique cracks of about 45°. From the three different mathematical models of macroscopic and mesoscopic views, it is concluded that the effect of temperatures on salt rock is more significant after 90°C. This research is important for exploring the macroscopic and microscopic mechanics evolution of salt rock and provides a reference for determining the long-term mechanical strength of salt rock.

1. Introduction

Salt rock can create an ideal environment for the storage of underground oil and gas energy, and salt cavern energy storage is generally built in the salt rock ore layer with a depth of 1500 m [1]. However, with the rapid development of shallow favourable deposits, the development of salt cavern underground energy storage is expanded from shallow (buried depth < 1500 m) to deep (buried depth 1500-2500 m) and ultradeep (buried depth > 2500 m), during which the construction and operation of underground storage also face more complex geological conditions, such as high in situ stress and

high ground temperature. Therefore, it is very important to study the physical and mechanical properties of salt rock in a high-temperature environment to ensure the safe operation of storage.

Many scholars have done a lot of experimental research on the mechanical properties of salt rock under the influence of temperature. Gao et al. [2] carried out triaxial compression tests of salt rock under the temperature of 25°C, 50°C, and 100°C to study the variation of macroscopic mechanical parameters of rock mass with temperature from a macro perspective, and they found that the peak stress and elastic modulus of salt rock decreased with the increase of temperature.

Wu et al. [3] monitored the acoustic emission activities of salt rock in the process of thermal loading and explored the acoustic emission characteristics of rock at different stress stages under high temperatures. Kang et al. [4] designed the damage self-recovery test of salt rock and analyzed the damage and healing mechanism of salt rock from the perspective of crystal by using SEM technology. Under different temperatures and osmotic pressures, Yang et al. [5] carried out triaxial creep tests on calcium mirabilite salt rock and analyzed the influence of temperature on the creep process of calcium mirabilite. Because of the restriction of the test conditions, the temperature in the triaxial test of salt rock was not high (below 100°C), and the results had limitations.

In addition, the laboratory tests always try to explain the temperature effect from the macroscopic perspective, which cannot reflect the mesoscopic development of salt rock in the thermodynamic coupling process; the DEM makes up this defect and is widely used in the geotechnical engineering field. Shen et al. [6] used PFC^{2D} to simulate the dynamic failure process of shale rock under uniaxial compression and explored the evolution characteristics of microcracks in brittle shale failure under different stresses. Jiang et al. [7] used the discrete element method (DEM) to carry out triaxial simulation tests on structural sand and compared the results of numerical simulation and laboratory tests. Li et al. [8] applied the 3D-GBM model to PFC^{3D} to explore the micro-mechanical properties of salt rock practical scale and verified the effectiveness of this method. Based on the DEM, Li et al. [9, 10] adopted the thermal-mechanical creep constitutive model to explore the micromechanism of the influence of temperature on the creep behaviour of salt rock. Xu [11] and Liang et al. [12] used PFC^{2D} to establish the thermal-mechanical model and explored the fracture mechanism of granite under high temperature from a mesoscopic perspective. However, although the particle discrete element method has been widely used to analyze the damage evolution of rock mass, the research on the failure law of rock under a high-temperature environment is limited.

Given the complexity of rock and earth mass mesostructure and the limitation of the research, there is no accepted mechanical theory formed to characterize the relationship between macro- and mesoevolution of rock mass. Based on the particle flow simulation technology, this paper makes up for the inadequacy of indoor high-temperature rock mechanics tests, analyzes the triaxial compression failure process of salt rock under 20°C, 50°C, 90°C, 120°C, and 150°C, and systematically studies the correlation characteristics of salt rock from mesoscopic change to macroscopic response, revealing the macro-mesoevolution mechanism of salt rock damage under high-temperature environment.

2. Constitutive Contact Model and Thermal Module Implementation

2.1. Selection of Constitutive Model

- (1) Burger model: Burger's model is an elastoviscous rheological model, which consists of the Maxwell body in series with the Kelvin body (Figure 1(a)).

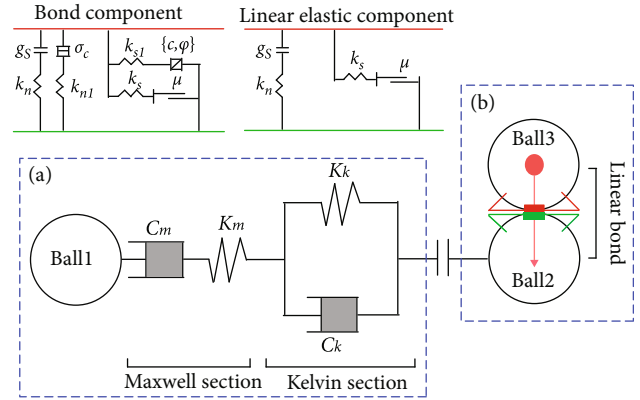


FIGURE 1: A combinatorial constitutive contact model of Burger and Linearbond.

The main contact parameters are the stiffness (K_m , K_n) of the elastic element and the bond coefficient (C_m , C_k) of the viscous element. The stiffness of the elastic element is the stiffness of contact between particles. The bond coefficient of the viscous element is the contact damping of the particles, which is related to the deformation strength. This model can well reflect the viscoplastic deformation characteristics of salt rock; however, during heating and loading, the internal thermal damage of the salt rock cannot be reflected by Burger's model, and the built-in program of the model does not have related functions, such as crack control network, force chain, and energy

- (2) Linearbond model: the Linearbond model consists of a bond component and a linear elastic component (Figure 1(b)), which establishes an elastic contact and can better simulate the linear elastic stage of salt rock. In addition, stiffness ratio (k_n/k_s), bond strength (c), and effective modulus (E^*) are the main contact parameters in the Linearbond model. The stiffness ratio is the ratio of normal stiffness to tangential stiffness (related to particle deformation). Bond strength is the contact bond strength of the particles. Effective modulus is the elastic modulus assigned to a single particle at the microscopic scale. After the contact bond is broken, the model allows the contacts between particles to produce cementation failure points, which can simulate the microcrack propagation during loading to better reflect the degradation of mechanical properties of rock and thermal expansion effects
- (3) Combination constitutive model: during the triaxial compression test, the salt rock exhibits strong viscoplastic deformation characteristics, and microcracks grow significantly. In addition, the high temperature increases the ductility of the rock mass, and the thermal response of the internal cementation is strong. When the temperature reaches a certain value, the salt rock may enter a creep stage. Therefore, to better simulate the mesoscopic failure process of salt rock

under high-temperature triaxial stress, the combination constitutive contact model of Burger and Linearbond was adopted, as shown in Figure 1. The constitutive models, burger and linear bond, and their parameters are quoted from the built-in database of PFC^{2D} of Itasca commercial [13, 14]

2.2. Heat Transfer Mechanism of the Model. To study the displacement and stress changes of rock particles under the action of thermal effect, the model needs to have the ability of heat storage and heat conduction. In the particle flow program, the heat conduction between particles is realized by the heat source through the heat pipe and finally forms the network heat transfer channel. The heat pipe represents the heat transfer process, which is related to predetermined thermal parameters of the model. Thermal parameters include thermal expansion coefficient (α), thermal resistance (η), thermal conductivity (k^*), and specific heat capacity (C_v). These parameters work together to generate heat conduction between particles. These parameters are determined following Section 3.4 of this paper. The thermal effect of particles produces the following effects: thermal strain causes particle expansion, which leads to the change of contact force; at the same time, the heat transferred through the contact between particles causes the expansion of the bond; their combined effect causes rock sample deformation. In addition, when heat is transferred to the inside of the model, the force and range of contact between particles will increase, and the parallel bond between particles will be broken, or particles will be moved, resulting in partial failure of the heat pipes between particles. The number of effective heat pipes decreases, and the overall heat conduction ability of the model decreases. The above process is consistent with the actual situation [15], so the PFC^{2D} model can better simulate the heat conduction process of rock.

2.3. Thermal Strain Constitutive Model. In the PFC^{2D}, the heat source completes heat conduction through the heat pipe and finally forms a network heat transfer channel. We assume that the effect of strain on temperature can be ignored, and the continuity equation of heat conduction involving thermal-mechanical coupled quasistatic mechanics is shown in

$$-\frac{\partial q_i}{\partial x_i} + q_v = \rho C_v \frac{\partial T}{\partial t}, \quad (1)$$

where q_i is the heat flow vector, q_v is the volumetric heat source intensity or energy density, ρ is the density, C_v is the specific heat capacity, and T is the temperature.

In the PFC^{2D}, the thermal strain is obtained by calculating the expansion of the adhesion between particles, and the thermal strain of the particles under the action of temperature is calculated by

$$\Delta R = \alpha R \Delta T, \quad (2)$$

where ΔT is the temperature increment, α is the linear expansion coefficient of the particle, and ΔR is the change in radius under temperature.

3. Numerical Modeling and Parameter Calibration

3.1. The Establishment of the Geometric Model. Referring to the high-temperature triaxial compression test in the salt rock chamber [16], numerical simulation was carried out to perform comparative analysis and verify the conclusion drawn in numerical simulation. The two-dimensional plane stress model was established, and the size of the model is $\Phi 100 \text{ mm} \times 200 \text{ mm}$, which is consistent with the laboratory test. In the model, the particle size range is $0.7 \text{ mm} \sim 1.05 \text{ mm}$, obeying uniform probability distribution. The reasonable ratio of the sample size to the average grain diameter is greater than 30~40 [17]. The combination constitutive model is adopted to simulate the contacts between particles; the contacts between the wall and the particle adopt Linear's model, forming a total of 17,993 contacts. The density of the rock sample is 2300 kg/m^3 , and the porosity is 0.03. The salt rock model is shown in Figure 2.

3.2. Test Scheme of Numerical Simulation. The first step is to calibrate the parameters of the constitutive contact model based on the laboratory test results. The test temperature was set to 20°C (indoor temperature), and the axial loading speed was set to 0.05 m/s . In the quasistatic simulation, a higher local damping coefficient is usually used to remove the kinetic energy in the system effectively, making the quasistatic deformation occur at a much higher rate than the actual situation [18, 19]. Triaxial compression tests with confining pressures of 10 MPa, 20 MPa, and 30 MPa were, respectively, simulated to obtain the stress-strain curves; data processing was studied by trial and error method and comparison method. Then, the results were compared with laboratory test results to confirm the reasonable parameters of the numerical simulation constitutive contact model.

The second step is to determine the thermal model parameters and the new contact parameters. The triaxial compression tests were carried out at environment temperatures of 50°C , 90°C , 120°C , and 150°C while setting the triaxial confining pressure as 10 MPa and the axial loading speed as 0.05 m/s . Through parameter optimization, the stress-strain curves of salt rock were obtained. By comparing to laboratory test results, the reasonability of numerical simulation thermal model parameters was verified, and new contact parameters were determined.

The third step is to conduct the triaxial high-temperature numerical simulation test of salt rock. According to the parameters determined above, the triaxial confining pressure was set to be 10 MPa, and the axial loading speed was set to be 0.05 m/s . The stress-strain curves of salt rock under the environment temperatures of 20°C , 50°C , 90°C , 120°C , and 150°C were to obtain to further explore the damage evolution mechanism and macroscopic and mesoscopic characteristics of salt rock model at high temperatures.

3.3. Determination of Constitutive Contact Model Parameters. Since the cross-sectional area of the salt rock changes greatly after compression, the assumption of small strain is no longer applicable. Therefore, based on the results of the laboratory test [16], the area correction method [20] was used to process

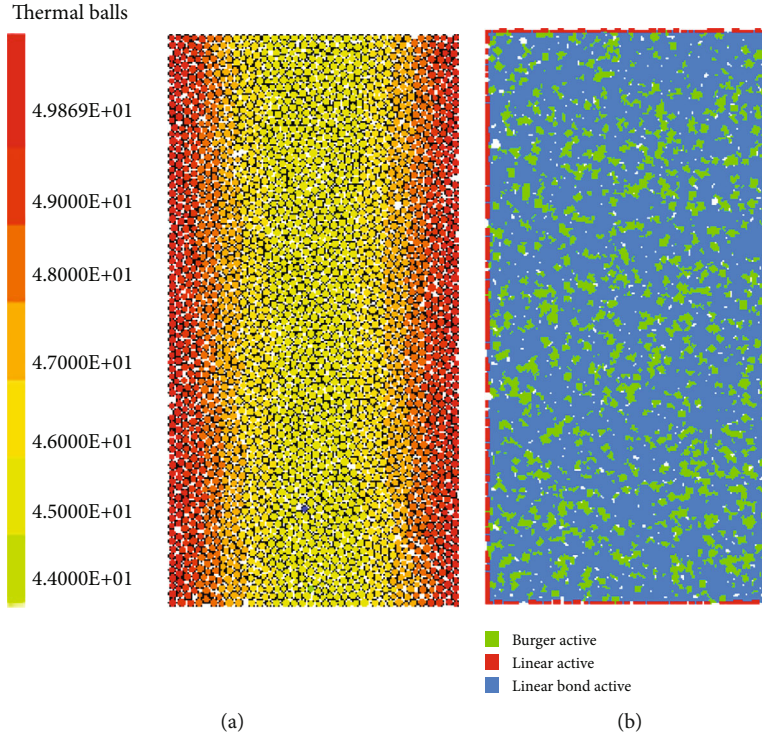


FIGURE 2: Numerical model of the salt rock: (a) particle model of heat transfer; (b) different contact models between particles.

the stress-strain data (Figure 3). The principle of the area correction method is as follows.

As the deformation changes the cross-sectional area of the rock sample, the corresponding pressure can be corrected by engineering strain; the specific expression is as follows.

$$\sigma_{\text{luc}} = \frac{F_1}{A'}, \quad A' = \frac{A_0}{1 - \varepsilon_t}, \quad (3)$$

where σ_{luc} is linear corrected axial pressure, A_0 is the cross-sectional area of the unpressurized sample, F_1 is the axial force, and ε_t is the engineering strain value.

In addition, according to the current research results [21–25], a set of constitutive model mesoparameters (Table 1) are determined by comparing the revised laboratory test results of salt rock so that the basic macroscopic parameters and stress-strain curves from the triaxial numerical simulation at room temperature are in good agreement with the laboratory test results (Figure 3). Comparison of stress-strain curves between laboratory test and numerical simulation shows that the correlation coefficients between the test curves and numerical curves are 0.9652, 0.9402, and 0.9601, respectively. The selected mesoparameters can reasonably reflect the macromechanical properties of the laboratory triaxial tests.

3.4. Determination of Thermal Model Parameters and New Contact Parameters. The heat conduction of the salt rock model was simulated by using the heat module of PFC^{2D}, in which the upper and lower boundary of the salt rock model was set to be adiabatic, so the heat was transmitted

from the lateral boundary of the model. With the reference data [9, 26, 27] and optimized parameters, a set of mesoscopic parameters of the thermal model were determined (Table 2). Specific heat capacity, C_v (J/kg°C), indicates the amount of heat required to raise the temperature of 1 kg of material by 1°C. The microscopic properties could be the same as the macroscopic specific heat capacity of the material. The thermal coefficient of expansion, α (1/°C), is the relative change in length of a unit length object when its temperature increases by 1°C. This microscopic property can be set by the macroscopic thermal coefficient of expansion α of the material. Upper and lower boundary thermal resistance, η (°C/W·m), is the ratio of the temperature difference between the two ends of the object and the power of the heat source when heat is transmitted through the object. The value of η can be calculated by traversing the thermal network of a given granular material. Macroscopic thermal conductivity, k^* (W/m°C), refers to the heat transfer per unit time through per unit horizontal cross-sectional area when the temperature gradient is 1°C/m vertically downward.

In addition, as the temperature rose, the cohesion between the particles was weakened, the particles moved, and the cementation points were destroyed, resulting in the contact of the particles, the local organization, and even the overall structure greatly changed. Therefore, it is necessary to update the contact parameters of the model after the rock temperature rising to better simulate the loading process of salt rock after heating up. The contact model parameters at 20°C were used as the reference parameters, and the new contact parameters were determined through

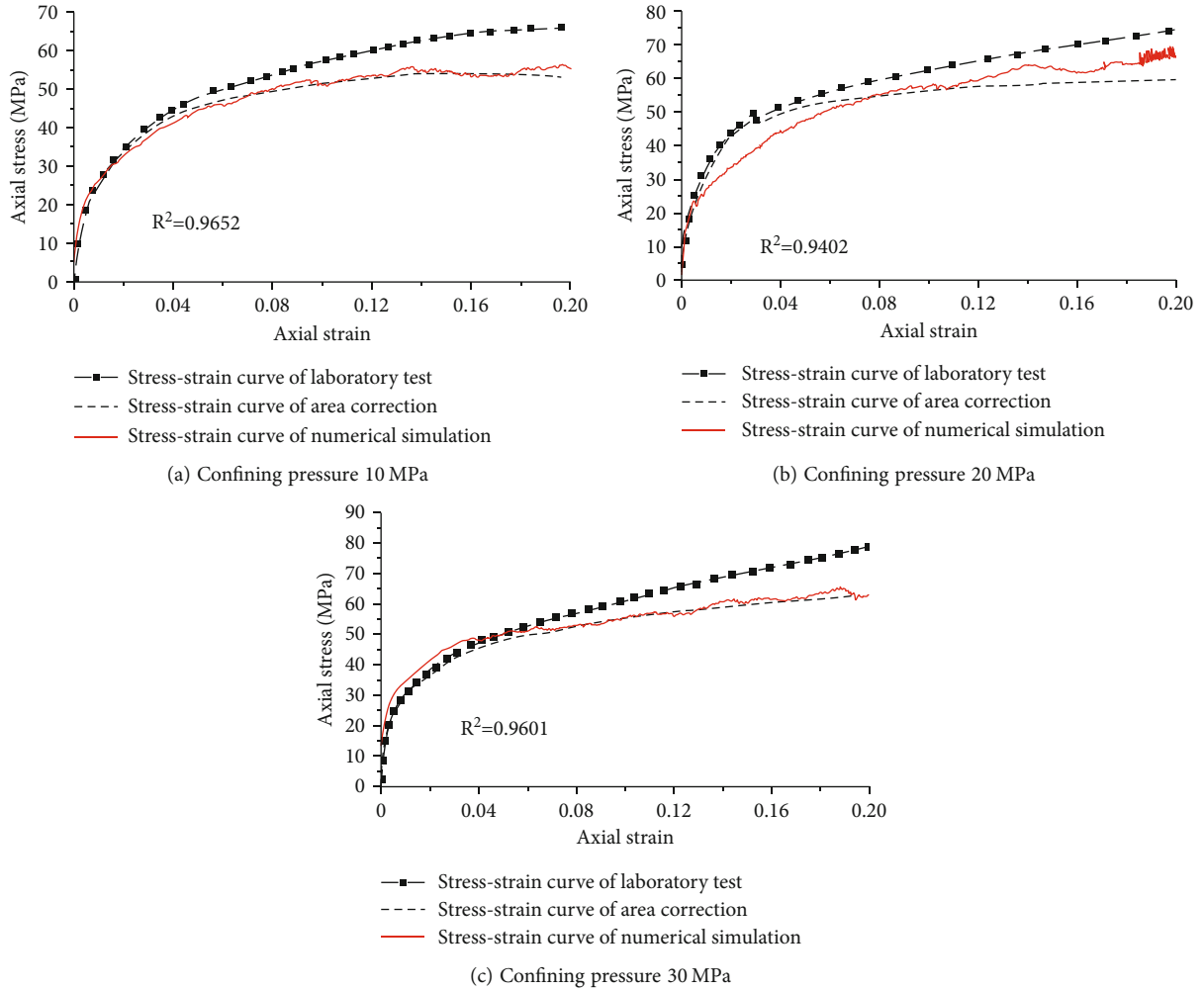


FIGURE 3: Stress-strain curves of different confining pressures at 20°C: (a) confining pressure 10 MPa; (b) confining pressure 20 MPa; (c) confining pressure 30 MPa.

TABLE 1: Microstructure parameters of PFC^{2D} constitutive contact model.

Contact model	Mesoscopic parameter	Numerical value
Linear	Density (kg/m ³)	2300
	Linear contact modulus (Pa)	3 × 10 ⁹
	Stiffness ratio k_n/k_s	1.0
	Coefficient of intergranular friction (μ)	0.6
Parallel bond	Bond contact modulus (Pa)	3 × 10 ⁹
	Normal bond strength (Pa)	2.6 × 10 ⁸
	Shear bond strength (Pa)	2.0 × 10 ⁸
Burger's	Kelvin elastic coefficient (Pa)	1 × 10 ⁹
	Kelvin viscosity coefficient (Pa·s)	1 × 10 ⁵
	Maxwell elastic coefficient (Pa)	5 × 10 ¹¹
	Maxwell viscosity coefficient (Pa·s)	1 × 10 ⁷
	Friction coefficient (μ)	0.6

TABLE 2: Microstructure parameters of PFC^{2D} thermal model.

Model parameter	Units	Numerical value
Coefficient of thermal conductivity (k^*)	W/(m°C)	2.5
Specific heat capacity (C_v)	J/kg°C	1015
Thermal coefficient of expansion (α)	1/°C	2.8×10^{-6}
Upper and lower boundary thermal resistance (η)	°C/W · m	1×10^{300}

TABLE 3: New contact parameters of rock sample model at high temperature.

Model parameter	Numerical value				
	20	50	90	120	150
Temperature (°C)					
Kelvin elastic coefficient (Pa)	1×10^9	5×10^8	2.5×10^8	2.2×10^8	2.0×10^8
Maxwell elastic coefficient (Pa)	5×10^{11}	4×10^{11}	3.0×10^{11}	2.5×10^{11}	1.5×10^{11}
Maxwell viscosity coefficient (Pa·s)	1×10^7	0.8×10^7	0.6×10^7	0.4×10^7	0.2×10^7
Normal bond strength (Pa)	2.6×10^8	2.4×10^8	2.2×10^8	2.0×10^8	1.8×10^8
Shear bond strength (Pa)	2.0×10^8	1.8×10^8	1.7×10^8	1.54×10^8	1.4×10^8

parameter optimization (Table 3). Under temperatures of 50°C, 90°C, 120°C, and 150°C, the simulation results of salt rock experiments with confining pressure of 10 MPa were obtained (Figure 4). The stress-strain characteristics of the laboratory test and numerical simulation test show good agreement, which verifies the rationality of the selection of thermal parameters and new contact parameters.

4. Analysis of Numerical Calculation Results

4.1. Characteristic Analysis of Salt Rock Strain Curves. In this section, triaxial compression simulations were carried out on salt rock under a different confining pressure of 10 MPa and 20°C, 50°C, 90°C, 120°C, and 150°C, respectively. The transverse strain, stress-strain curves, and volume strain curves of the samples were monitored and recorded, as shown in Figures 5–7.

Generally, the deformation process of rock can be divided into a linear elastic stage, a nonlinear elastic stage, a plastic stage, and a failure stage. As shown in Figure 5, the turning point from the nonlinear elastic stage to the plastic stage is defined as the elastic limit point, and it can be seen that the elastic limit points (a–e) of the rock gradually descended with the increase of temperature. The result shows that with the increase of temperature, the plastic deformation of salt rock becomes more obvious, and the stress-strain curves of salt rock tend to be flatter. Figure 6 shows that with the temperature increase from 20°C, 50°C, 90°C, 120°C, to 150°C, respectively, the dilatancy points (a–e) of salt rock continuously increase at 20°C, 50°C, 90°C, 120°C, and 150°C. The result shows that with the increase of temperature, the internal particles of the rock sample expand, which causes the volume to increase and the same sample becomes loose. Therefore, the volume strain values of the sample reaching the expansion points increase during axial loading.

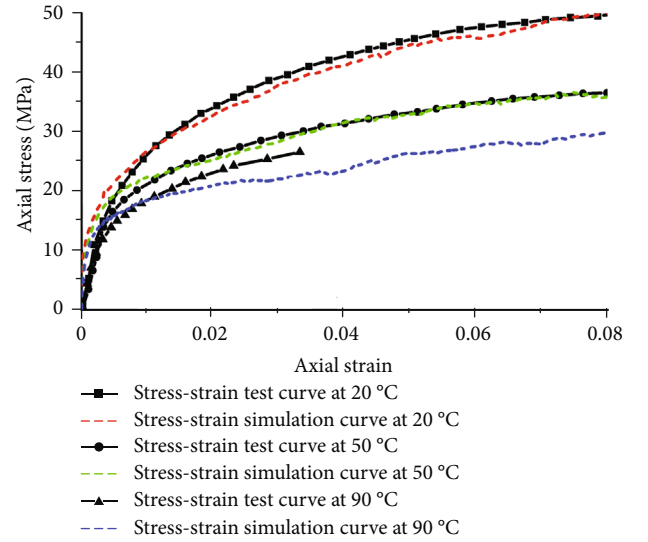


FIGURE 4: Stress-strain curves of different temperatures under the confining pressure of 10 MPa.

Figure 7 shows the transverse strain of salt rock after heating, and it can be seen that with the increase of termination temperature, the transverse strain was 0.0147, 0.0170, 0.018, and 0.0182, respectively, and the corresponding increments were 0.0023, 0.001, and 0.0002; this can be explained as that the temperature causes the increase of thermal motion of particles. However, when the particles collided with the wall, particles moved in reverse, resulting in the decrease of the increments of transverse strain.

4.2. Evolution of Force Chain Network in Rock Mass during Loading. The force chain network represents the distribution of the interparticle contact force in the soil framework

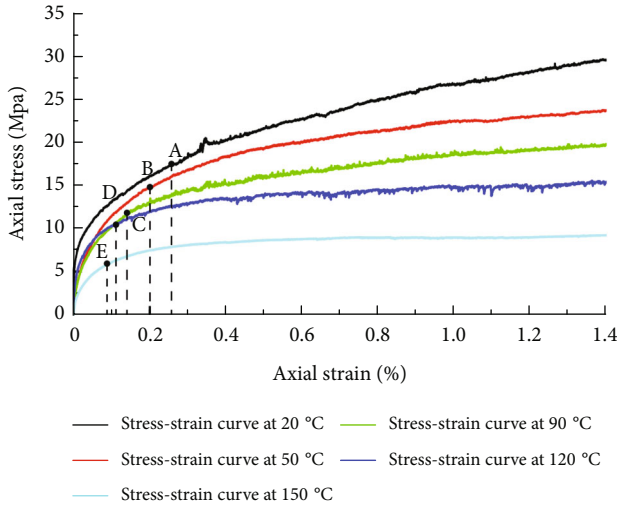


FIGURE 5: Stress-strain simulation curves of salt rock samples at different temperatures.

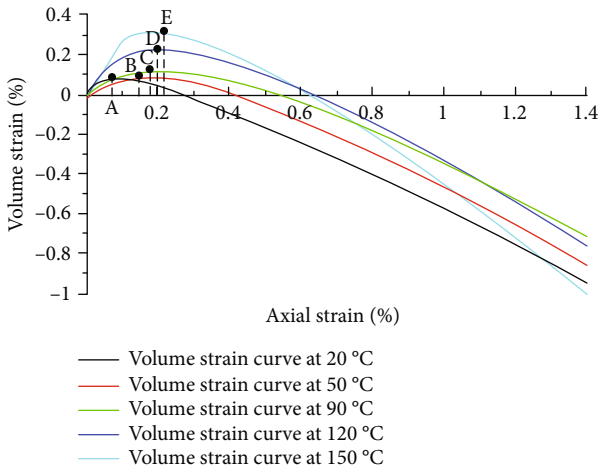


FIGURE 6: Volume strain simulation curves of salt rock samples at different temperatures.

system, which can reflect the sensitivity of the particle system to the force. Figure 8 shows the variation of the force chain network of the sample at different temperatures under the axial strain of 0.15. The contact force in the force chain was generalized to visually reflect the variation of the internal stress field of the sample at different temperatures.

- (1) It can be seen from Figures 8(a)–8(e) that the contact force inside the salt rock gradually decreased, and the strong chains broke and disappeared with the damage of the samples; at the same time, as the temperature increased, the proportion of weak chains increased under the same strain of 0.15, showing that the high temperature intensifies the rupture of contact between particles in the salt rock
- (2) The maximum contact force changed from 0.787 MPa to 0.649 MPa as the temperature changed from 20°C to 50°C. When the temperature changed from 120°C to 150°C, the maximum contact force varied from

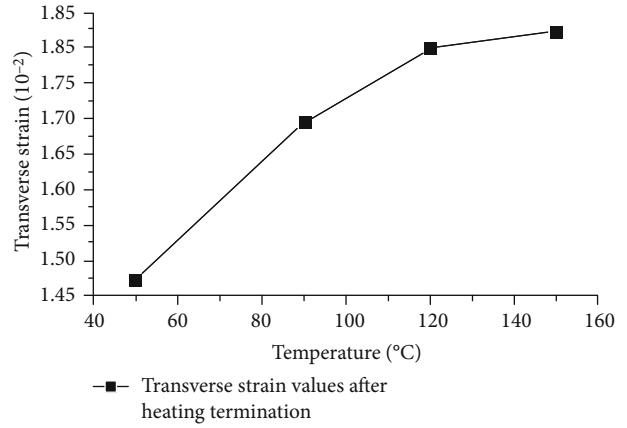


FIGURE 7: Transverse strain values of salt rock model after heating termination.

0.6 MPa to 0.417 MPa. For the temperature of 50°C, 90°C, and 120°C, the contact force slightly changed from 0.649 MPa, 0.62 MPa, to 0.6 MPa. However, Figures 8(b)–8(d) show that the force chains inside the rock sample significantly became disperse from 50°C to 120°C, indicating that the damage began to intensify gradually. The contact force decreased sharply at 150°C, indicating that the salt rock was damaged significantly

4.3. Evolution Law of Cloud Image of Displacement Field inside the Model. Figure 9 shows the change of displacement field in the sample under the temperature of 20°C, 50°C, 90°C, 120°C, and 150°C, respectively, and the axial strain was 0.15.

- (1) By analyzing the displacement direction of particles, it can be known that the displacement direction of the particles in the middle of the sample showed an obvious radial expansion trend at different temperatures, and the salt rock model appeared a “drum shape” destruction phenomenon
- (2) The arrows in Figures 9(a)–9(e) indicate the outward expansion direction of the central particles. It can be seen that the expansion direction from the middle of the sample to the left and right ends was 12.08°, 9.55°, 8.2°, 6.3°, and 0°, respectively, with the increase of temperature, which gradually changed from incline to horizontal. Therefore, during the loading, the phenomenon of “drum shape” in the middle of the rock sample became more obvious with the increase of temperature

4.4. Expansion Analysis of Mesofailure of Rock Mass during Heating. This section studies the initiation and evolution of thermal cracks in the salt rock during the heating process when the confining pressure of the test is 10 MPa, the initial temperature of the test is 20°C, and the heating termination temperatures are 50°C, 90°C, 120°C, 130°C, and 150°C, respectively. Figure 10 shows the distribution and extension of thermal cracks inside rock samples when the temperature

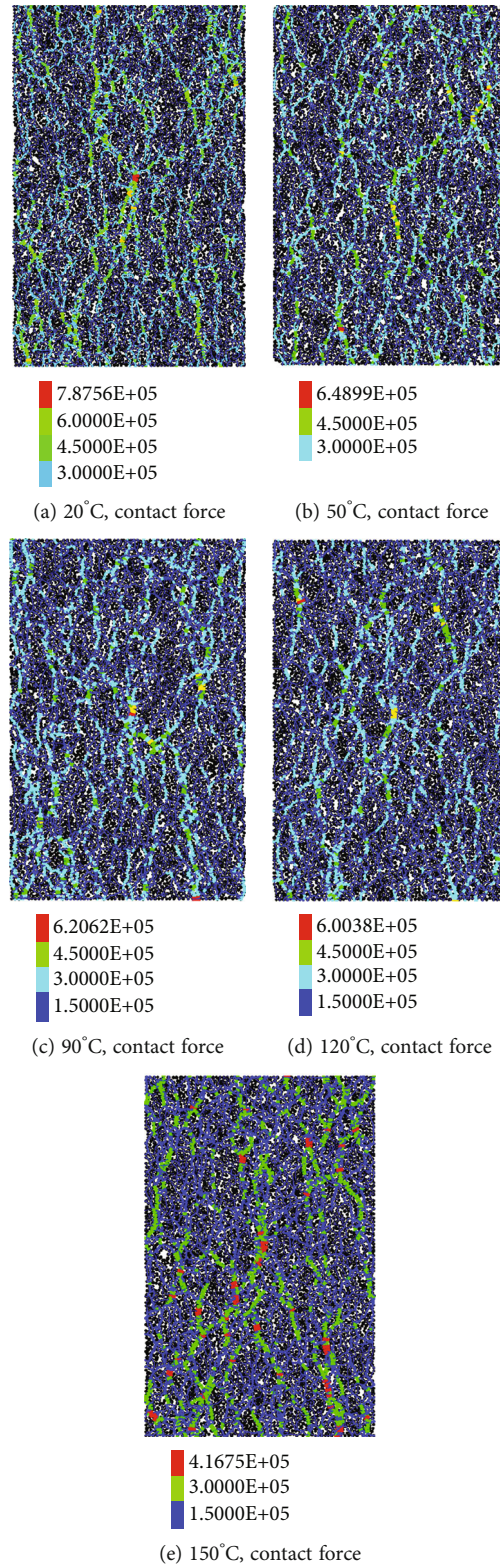


FIGURE 8: The force chain network evolution diagram of salt rock samples at different temperatures.

changed from 20°C to 50°C. A certain bonding distance is set between particles. The bonding force will be generated between particles due to the bonding action, which is called

the state of cementation when the distance between two particles is smaller than this distance. Cementation failure occurred under the action of thermal stress and thermal

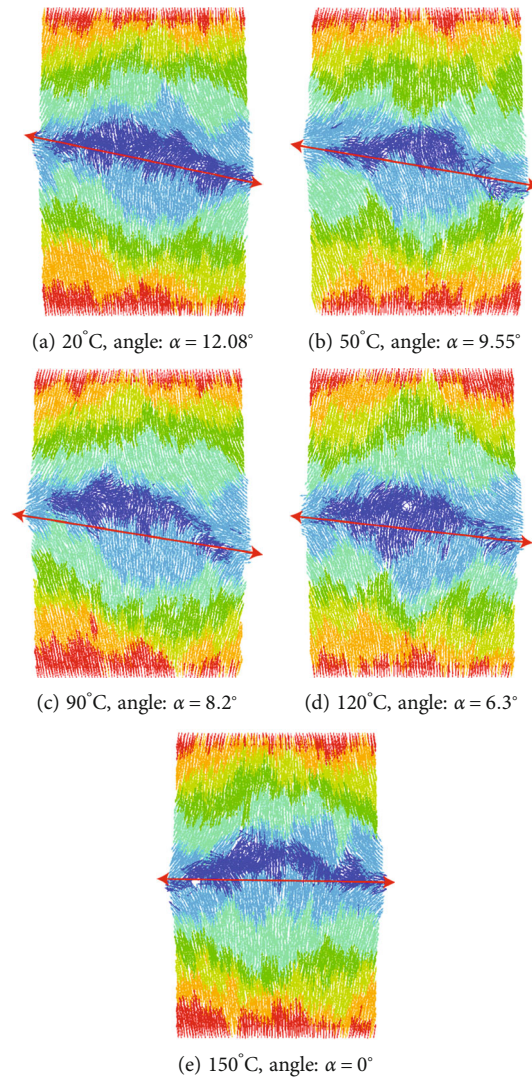


FIGURE 9: Displacement field nephograms of sample model at different temperatures.

strain. The failure criterion is as follows: the failure occurs between particles, generating cementation failure point, when the tensile stress, compressive stress, or shear stress generated between particles is greater than the cementation strength between particles.

the top and bottom of the model, the cementation failure points expanded obliquely, and the direction was about 45° from the horizontal direction

- (1) It can be seen from Figures 10(a)–10(e) that there was a temperature gradient between the boundary and the internal particles of rock mass, and the cementation failure occurred first at the edge of the sample under the combined effect of thermal stress and thermal strain. As the heat was transferred to the interior of the model, the number of cementation failures increased, and the cementation failure points near the edge of the sample gradually connected. After reaching the termination temperature, the cementation failure points became stable
- (2) In the middle of the model, the cementation failure points expanded along the transverse direction. At

- (3) Figure 11 shows the curve of the number of cementation failures under different temperatures. Figure 11 (a-b1-c1-d1) is the segment point of the cementation failure curve at 50°C, and Figure 11 (a-b2-c2-d2) is the segment point of the cementation failure curve at 90°C, 120°C, 130°C, and 150°C. It can be seen that at the initial stage of temperature rising (a-b1 and a-b2), the number of internal cementation failures in the salt rock increased linearly. With the transmission of heat (b1-c1 and b2-c2), the internal temperature gradient of rock mass became smaller, and the number of cementation failures grew smoothly. However, with the increase of temperature, the thermal motion of the particles increased, the cohesion decreases, and the

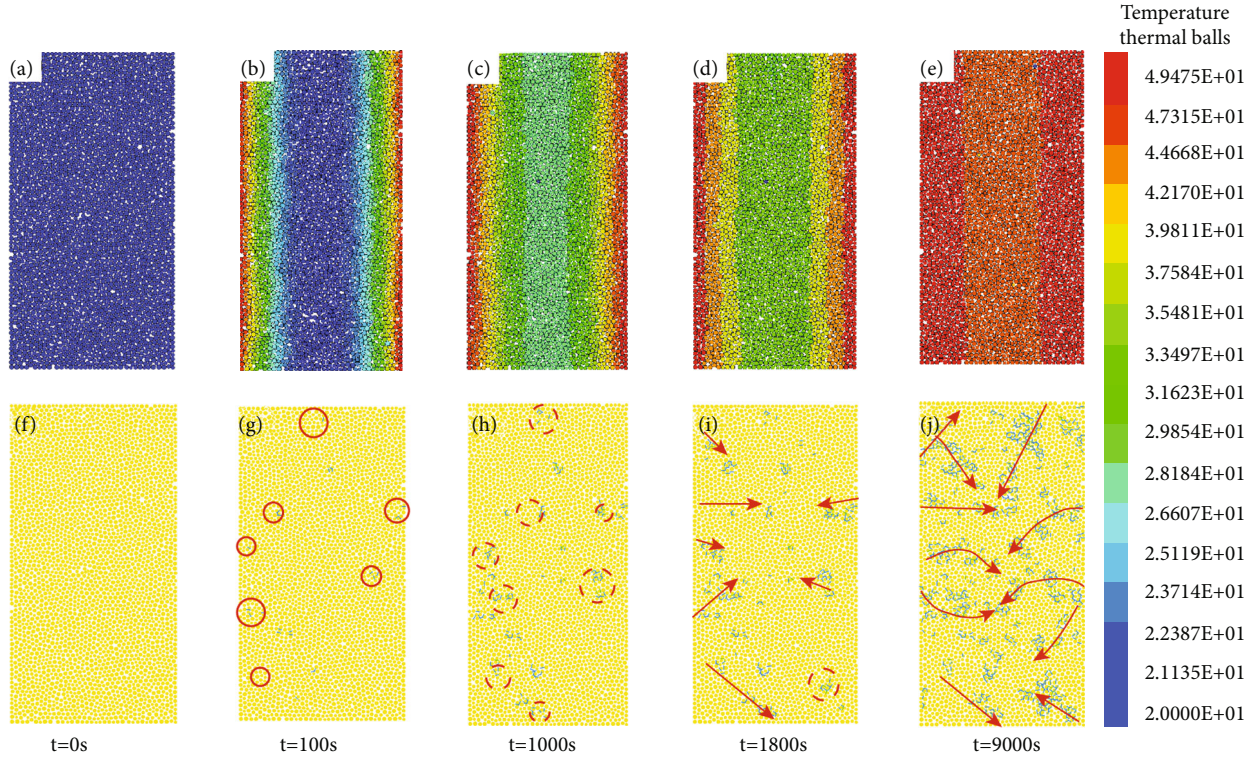


FIGURE 10: Distribution and propagation of cementation failure points in the salt rock model at 50°C (blue is the tensile failure points, green is the shear failure points, and red arrow represents the microcrack propagation direction).

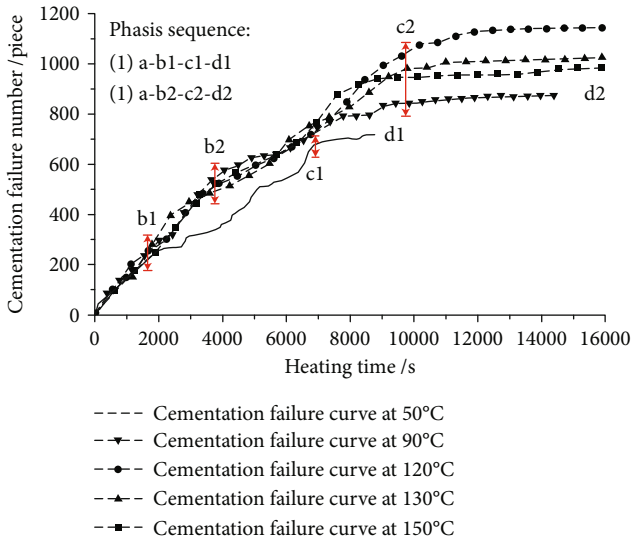


FIGURE 11: Cementation failure curves of sample model at different temperatures during temperature rising.

cementation failure points continued to increase at a slower rate. After the termination of heat transfer (c1-d1 and c2-d2), the cementation failure of rock mass no longer increased

- (4) According to the statistics of rock cementation failure points during the whole process of heating (Table 4), it was found that the number of cementation failure

points gradually increased with the termination temperature. However, when the temperature exceeded 120°C, the number of cementation failure points decreased, which may be because the significant enhancement of thermal movement and diffusion of particles in this temperature range move particles no longer a single movement, but a granular organizational movement. At the same time, the wall became more sensitive to the movement of particles, and the confining pressure of the wall also largely prevented contact fractures caused by particle dislocations

5. Quantitative Analysis of Thermal Damage of Salt Rock

5.1. Damage Analysis Based on the Elastic Modulus. In this section, the damage value is defined by the change of elastic modulus of the sample before and after heating [28], and the damage variable $D(T)$ is calculated as follows.

$$D(T) = 1 - \frac{E_T}{E_0}, \quad (4)$$

where E_T is elastic modulus at temperature T (MPa) and E_0 is elastic modulus at 20°C (MPa).

By analyzing the stress-strain curves at 20°C, 50°C, 90°C, 120°C, and 150°C, the corresponding elastic modulus of salt rock was calculated to be 4.989 GPa, 4.56 GPa, 3.72 GPa, 2.33 GPa, and 1.089 GPa, respectively. $D(T)$ at different temperatures were 0, 0.0860, 0.2543, 0.533, and 0.7817, respectively,

TABLE 4: Cementation failure number of sample model at different temperatures.

Serial number	Initial temperature (°C)	Termination temperature (°C)	Cementation failure numbers (piece)
1#	20	50	720
2#	20	90	874
3#	20	120	1148
4#	20	130	1041
5#	20	150	998

and the change curves of damage variables and elastic modulus with temperature are drawn in Figure 12.

It can be seen that the elastic modulus gradually decreased with increasing temperature, while the damage variables gradually increased, showing a negative correlation of them. Before reaching 90°C, the damage variables increased slowly from 0 to 0.2543 by 0.2543, and after 90°C, it increased by 0.5274. Between 90°C and 120°C, the damage variables changed from 0.2543 to 0.5330 by 0.2787. From 120°C to 150°C, they changed from 0.533 to 0.7817 by 0.2487. In conclusion, the damage of the salt rock model was relatively gentle before 90°C, while the influence of temperature on the salt rock was more significant after 90°C, but the higher the temperature did not cause more damage.

5.2. Damage Analysis Based on Cementation Accumulation Numbers. The particles are connected by the Linearpbond model and the Burger model. When the contact force is greater than the bonding strength, the contact bond will be broken and produce cementation failure points; then, the cementation failure points extend and penetrate each other to form microcracks, finally leading to the damage and deterioration of the salt rock model.

In addition, the rock damage index is usually defined by the development of microcracks as the basic variable. However, in the actual test, the number of cracks is not easy to obtain [29]. Therefore, many scholars define the damage variables as the ratio of cumulative acoustic emission ringing numbers to the cumulative ringing numbers under peak stress [30, 31]; the cementation failure numbers can represent cumulative acoustic emission ringing numbers in numerical simulation of particle flow [32, 33]. Therefore, with the particle flow discrete element method, the rock damage index was calculated as follows to quantitatively analyze the damage degree of salt rock at different temperatures.

$$D(T) = \frac{N(T)}{N_{0(T)}}, \quad (5)$$

where $N(T)$ is the cumulative cementation failure number at temperature T and $N_{0(T)}$ is the cementation failure number corresponding to peak stress at temperature T .

Generally, the point where the axial strain of salt rock is 0.1 is defined as the peak stress point. It can be seen from Figure 13 that at different temperatures, the variation trend

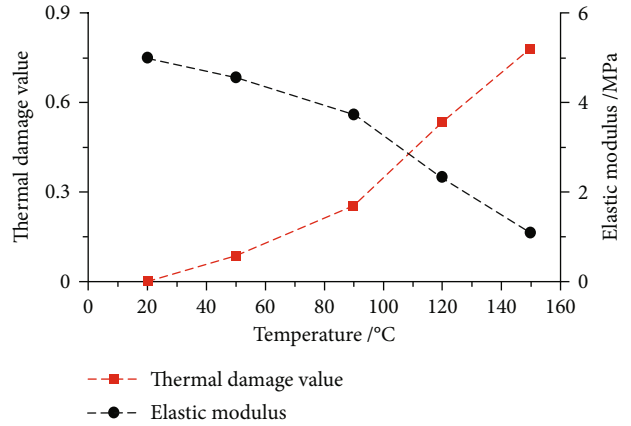


FIGURE 12: Damage variable curves of salt rock at different temperatures.

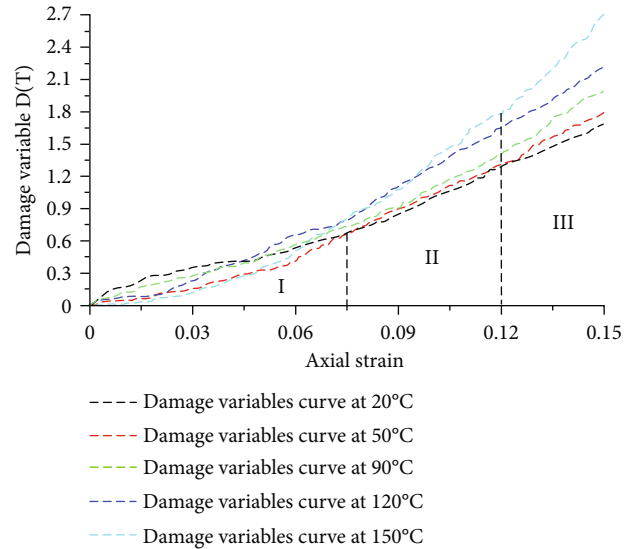


FIGURE 13: Variation curves of damage variables with axial strain at different temperatures.

of the salt rock damage variable $D(T)$ with the axial strain was basically the same, which can be divided into three stages. In stage I, the curve showed a slow-growth trend. In stage II, the slopes of all curves began to increase, and the damage started to be gradually intensified when the axial strain reached 0.075. In stage III, the damage variable sharply increased, and the higher the temperature, the more obvious the increment.

In the early stage of loading ($\varepsilon = 0 \sim 0.075$), the damage variable of salt rock did not change obviously at different temperatures. At the end of loading ($\varepsilon = 0.075 \sim 0.15$), the temperature showed a great influence on the damage of salt rock. In order to visually show the influence of temperature on the internal damage of salt rock, at different temperatures, the damage variables of salt rock when the axial strain was 0.09, 0.12, and 0.15 were obtained, as shown in Table 5.

TABLE 5: Damage variables of salt rock at different temperatures.

Temperature (°C)	Strain ($\epsilon = 0.09$)	Strain ($\epsilon = 0.12$)	Strain ($\epsilon = 0.15$)
20	0.7243	1.2949	1.6872
50	0.9192	1.3113	1.7962
90	0.9203	1.4162	1.9930
120	1.10	1.6432	2.2162
150	1.0645	1.7871	2.7097

It is found that from 20°C to 50°C, the damage increments under different strains were 0.1949, 0.0164, and 0.109, respectively. From 50°C to 90°C, the damage increments were 0.0011, 0.1049, and 0.1968, respectively. From 90°C to 120°C, the damage increments were 0.1797, 0.227, and 0.229, respectively. From 120°C to 150°C, the damage increments were -0.0355, 0.1439, and 0.4935, respectively. In conclusion, under different strains, the damage increments increase significantly with the temperatures after 90°C.

5.3. Damage Analysis Based on Crack Density Parameters. In the particle flow program, the rock model was established based on the assumptions of nonintersecting cracks, uniform crack distribution, and simple crack shape, which is the hypothetical model without cracks interaction (NIA). Based on NIA, Budiansky and O'Connell deduced the calculation model of rock elastic modulus and crack density parameters [34, 35], as follows.

$$\rho = \frac{45(2 - \nu_0)}{16(1 - \nu_0^2)(10 - 3\nu_0)} \left(\frac{E_0}{E} - 1 \right), \quad (6)$$

where E_0 is the elastic modulus of undamaged rock (MPa), ν_0 is Poisson's ratio of undamaged rock, E is the elastic modulus of damaged rock (MPa), and ρ is the crack density parameters.

Referring to the elastic modulus and Poisson's ratio of undamaged salt rock at room temperature, this paper explored the damage degree of salt rock at 20°C, 50°C, 90°C, 120°C, and 150°C. The elastic modulus and Poisson's ratio of undamaged salt rock are 7.157 MPa and 0.187, respectively [16]. Formula (3) is used to calculate the crack density of salt rock at different temperatures (see Table 6) and draw the curve of crack density with temperature, as shown in Figure 14.

When there is no thermal damage, the crack density parameter of rock is set to 0. It can be seen from Figure 14 that the crack density parameters increased slowly from 0.2433 to 0.5172, totally by 0.2739 before 90°C. From 90°C to 120°C, the value changed from 0.5172 to 1.1597 by 0.6425. From 120°C to 150°C, it changed from 1.1597 to 3.1192 by 1.9595. It can be seen that the number of cracks in the unit volume sharply increased after 90°C, and the temperature had a significant impact on the damage of salt rock at 150°C.

TABLE 6: Crack density parameters of salt rock at different temperatures.

Temperature (°C)	Elastic modulus (MPa)	Crack density parameters
20	4.989	0.2433
50	4.56	0.3188
90	3.72	0.5172
120	2.33	1.1597
150	1.089	3.1192

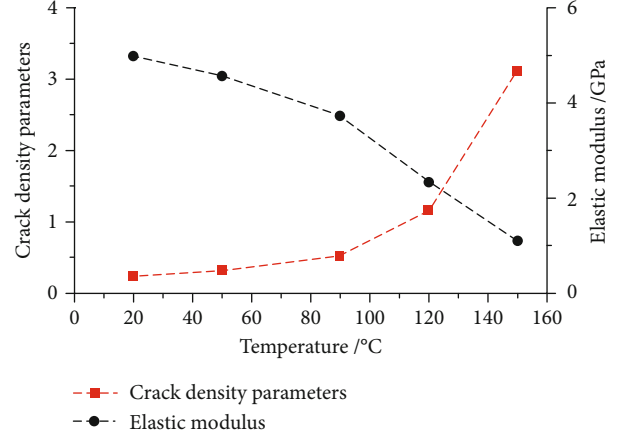


FIGURE 14: Crack density parameter curve of salt rock at different temperatures.

5.4. Comparative Analysis of Calculation Models. The elastic modulus, cumulative cementation numbers, and derived crack density parameters are closely related to the damage deterioration of rock mechanical properties.

- (1) The elastic modulus and crack density showed a consistent variation with temperature, indicating that the temperature has a significant effect on the damage of salt rock after 90°C
- (2) According to the calculation of cementation accumulation numbers, it was found that the damage of salt rock gradually increased after the axial strain reaching 0.075. Under different strains, the increments were 0.196, 0.1213, and 0.3018 from 20°C to 90°C, while the increments were 0.1442, 0.3079, and 0.7225, respectively, from 90°C to 150°C. After 90°C, the damage variables increased significantly with the change of temperatures; with the increase of loading, the damage variables increased significantly at 150°C. In addition, the crack density parameter also represents the damage of salt rock from the perspective of microcracks. The crack density parameter increased by 0.2739 from 20°C to 90°C, while it increased by 2.602 from 90°C to 150°C. After 90°C, the number of cracks per unit volume increased sharply. It can be seen from Figure 13 that the temperature has a significant effect on the

damage of salt rock at 150°C. The damage analysis of microcracks in salt rock from two different calculation models reflects the damage of salt rock under the action of temperature

- (3) Model ①: the calculation model is established from the perspective of macroscopic elastic modulus. Model ②: the calculation model is established from the perspective of mesoscopic cementation failure points. Model ③: the microcrack density parameter is established by using the macroscopic modulus, and the microphysical quantity characterizing the material is connected with the macroscopic modulus. From three different mathematical models, it is concluded that the temperature has a significant effect on the damage of salt rock after 90°C

6. Discussions

The physical and mechanical properties of the salt rock are affected by temperature, and the mechanism is complicated. On the one hand, the temperature is related to the thermal motion of the crystal particles. The higher the temperature, the weaker the binding force between particles, resulting in the enhanced plasticity of the rock and the decreased strength. The cohesion between rock particles is composed of true cohesion and apparent cohesion; true cohesion represents the bonding strength between particles, while apparent cohesion represents the frictional occlusal effect between particles [36]. In the low-temperature environment, the occlusal effect plays a dominant role, so the particle displacement is small, the elastic tensile deformation between the particles is not obvious, and the bonding strength is not weakened. In the high temperature, the friction and occlusion strength between particles are basically destroyed, and true cohesion plays a major role. With the increase of temperature, the bonding strength between particles is gradually destroyed, and the plastic deformation characteristics of rock become obvious. On the other hand, salt rock has damage repair function, including damage microcrack healing based on diffusion, microcrack filling based on NaCl crystal recrystallization, and the healing and bonding of NaCl crystal particles in the fracture zone [4]. The energy recovery, healing speed, and crystallization development of salt rock are closely related to the ambient temperature. The simultaneous occurrence of damage and repair of salt rock is also the reason for the complexity of the research topic. Through numerical simulation, it is found that there exists a postpeak hardening stage during triaxial compression of salt rock at high temperatures; the higher the ambient temperature, the more obvious this stage is. Due to the restriction of test instruments and high-temperature conditions, the curves of this stage generally cannot be obtained in laboratory rock mechanics tests. In this stage, the salt rock still has a higher load-bearing capacity, the stress increment is small, and the strain keeps increasing. In addition, it is found in the numerical simulation that the number of cementation failures in the salt rock model decreases when the temperature exceeds 120°C. Meanwhile, the damaged salt rock has short-term self-healing characteristics under temperature conditions in

laboratory tests. To sum up, the formation mechanism and physical significance of the above problems need to be further studied.

7. Conclusions

In this paper, through particle flow simulation analysis technology, the triaxial compression failure process and strength characteristics of salt rock under a high-temperature environment were systematically studied, and the following conclusions can be drawn.

- (1) With the increase of temperature, the elastic limit points (a–e) of rock gradually decrease, which indicates that the plastic deformation characteristics of salt rock become more obvious. In addition, as the termination temperature gradually increases, the transverse strain values are 0.0147, 0.0170, 0.018, and 0.0182, respectively, and the increments of transverse strain are 0.0023, 0.001, and 0.0002, which maybe because of the decrease of the increment of transverse strain caused by the limitation of the wall and confining pressure.
- (2) With the increase of temperature, the strong chains break and disappear, and the proportion of weak chains increase, which shows that the high temperature intensifies the rupture of contact between particles in the salt rock. The strength chains inside the rock sample decrease significantly from 50°C to 120°C, indicating that the damage begins to intensify gradually. The contact force decreases sharply at 150°C, indicating that the salt rock is damaged significantly at a temperature of 150°C during the loading process
- (3) By analyzing the displacement direction of particles in the cloud map of the displacement field, it can be known that the displacement direction of the particles in the middle of the sample shows an obvious radial expansion trend at different temperatures, and the salt rock model shows a “drum shape” destruction phenomenon. With the increase of temperature, the expansion direction from the middle of the sample to the left and right ends is 12.08°, 9.55°, 8.2°, 6.33°, and 0°, respectively, and the phenomenon of “drum shape” in the middle of rock sample becomes more obvious
- (4) During the heating process, the salt rock model is mainly controlled by tensile stress, so the thermal cracks in the sample are mainly tensile cracks. In the middle of the sample model, the microcracks roughly expand along the transverse direction. At the top and bottom of the model, the microcracks expand diagonally, and the direction of expansion is about 45° in the horizontal direction. In addition, the number of microcracks in the salt rock decreases when the temperature exceeds 120°C, which is different from the general rock, indicating that the damage self-healing phenomenon seems to occur in this temperature range

- (5) The damage variables of salt rock are analyzed from the macro and micro perspectives; it is concluded that the damage of salt rock is more significant after 90°C. In addition, it is found that the damage of salt rock is significantly aggravated at 150°C in the mathematical model of cumulative cementation numbers and crack density parameter, which is also consistent with the evolution law of the force chain network in salt rock

Data Availability

All data are available on request.

Conflicts of Interest

The authors declare no conflict of interests related to this article.

Acknowledgments

This research is supported by the Natural Science Foundation of Hebei Province of China (No. D2021210006), the Hebei Province Key Research and Development Program of China (No. 21374101D), and the Program for the Top Young Talents of Hebei Province Education Department (No. BJ2019011). The authors are thankful for all of the support for this basic research.

References

- [1] J. W. Chen, *Study on Temperature Effect and Meso-Mechanism of Salt Rock*, Graduate University of Chinese Academy of Sciences (Institute of Rock and Soil Mechanics), 2008.
- [2] X. P. Gao, C. H. Yang, W. Wu, and J. Liu, "Experimental study on influence of temperature effect on mechanical properties of salt rock," *Rock and Soil Mechanics*, vol. 37, no. 11, pp. 84–87, 2005.
- [3] G. Wu, S. T. Zhai, H. Sun, and Y. Zhang, "Experimental study on acoustic emission characteristics of salt rock at high temperature," *Chinese Journal of Rock Mechanics and Engineering*, vol. 33, no. 6, pp. 1203–1211, 2014.
- [4] Y. F. Kang, J. Chen, D. Y. Jiang et al., "Damage self-recovery characteristics of salt rock brine after immersion under different temperature conditions," *Rock and Soil Mechanics*, vol. 40, no. 2, pp. 601–609, 2019.
- [5] Y. L. Yang, W. G. Liang, X. Q. Yang, M. T. Cao, J. Li, and N. Xiao, "Study on temperature effect of creep under multi-field coupling action of glauberite salt rock," *Journal of China Coal Society*, vol. 45, no. 3, pp. 1070–1080, 2020.
- [6] H. M. Shen, Q. Li, X. Y. Li, and J. L. Ma, "Laboratory experiment and numerical simulation study on brittle failure characteristics of Longmaxi Formation shale under different stress conditions in southern Sichuan," *Rock and Soil Mechanics*, vol. 39, no. S2, pp. 254–262, 2018.
- [7] M. J. Jiang, A. N. Shi, J. Liu, and F. G. Zhang, "Three-dimensional discrete element analysis of mechanical properties of structured sand," *Chinese Journal of Geotechnical Engineering*, vol. 41, no. S2, pp. 1–4, 2019.
- [8] H. Li, H. L. Ma, X. L. Shi, J. Zhou, H. N. Zhang, and J. J. K. Daemen, "A 3D grain-based model for simulating the micromechanical behavior of salt rock," *Rock Mechanics and Rock Engineering*, vol. 53, no. 6, pp. 2819–2837, 2020.
- [9] W. J. Li, Y. H. Han, T. Wang, and J. W. Ma, "DEM micromechanical modeling and laboratory experiment on creep behavior of salt rock," *Journal of Natural Gas Science and Engineering*, vol. 46, no. 2, pp. 38–46, 2017.
- [10] W. J. Li, C. Zhu, C. H. Yang, K. Duan, and W. R. Hu, "Experimental and DEM investigations of temperature effect on pure and interbedded rock salt," *Journal of Natural Gas Science & Engineering*, vol. 56, no. 1, pp. 29–41, 2018.
- [11] Z. Y. Xu, *Study on Micro-Anisotropic Brittle Fracture Mechanism of Hard Rock under Thermal-Mechanical Coupling*, Chengdu University of Technology, Sichuan, 2014.
- [12] Y. K. Liang, Z. C. Feng, J. Bai, X. C. Li, and C. Wang, "Particle flow analysis of granite thermal fracture characteristics under thermodynamic coupling," *Water Resources and Power*, vol. 38, no. 1, pp. 127–130+193, 2020.
- [13] Itasca Consulting Group Inc, *PFC2D (Version 5.0) Users Manual*, Itasca Consulting Group Inc., USA, 2019.
- [14] H. Lin, W. H. Kang, J. Oh, I. Canbulat, and B. Hebblewhite, "Numerical simulation on borehole breakout and borehole size effect using discrete element method," *International Journal of Mining Science and Technology*, vol. 30, no. 5, pp. 623–633, 2020.
- [15] J. Kang, *Research and Application of Rock Thermal Fracture*, Dalian University of Technology Press, Dalian, 2008.
- [16] Z. Li, *Experimental Study on Mechanical Properties of Salt Rock under the Coupling of Stress and Temperature*, Chongqing University, Sichuan, 2012.
- [17] R. P. Jensen, P. J. Bosscher, M. E. Plesha, and T. B. Edil, "DEM simulation of granular media—structure interface: effects of surface roughness and particle shape," *International Journal for Numerical & Analytical Methods in Geomechanics*, vol. 23, no. 6, pp. 531–547, 1999.
- [18] X. B. Ding, L. Y. Zhang, H. H. Zhu, and Q. Zhang, "Effect of model scale and particle size distribution on PFC3D simulation results," *Rock Mechanics and Rock Engineering*, vol. 47, no. 6, pp. 2139–2156, 2014.
- [19] X. Cai, Z. Zhou, and X. Du, "Water-induced variations in dynamic behavior and failure characteristics of sandstone subjected to simulated geo-stress," *International Journal of Rock Mechanics and Mining Sciences*, vol. 130, article 104339, 2020.
- [20] G. Wang, L. Z. Xie, Z. M. Hou, J. F. Liu, and W. Xing, "Comparative study on rock salt triaxial compression test methods and data processing methods," *Rock and Soil Mechanics*, vol. 35, no. 2, pp. 429–434+458, 2014.
- [21] C. Shi, Q. Zhang, and S. N. Wang, *Numerical Simulation Technology and Application of Particle Flow*, China Construction Industry Press, Beijing, 2018.
- [22] S. Li, Y. Liu, and K. J. Wu, "Study on discrete element numerical simulation and meso deformation mechanism of sand direct shear test," *Journal of Yangtze River Scientific Research Institute*, vol. 34, no. 4, pp. 104–110+116, 2017.
- [23] C. Shi and W. Y. Xu, *Numerical Simulation Technique and Practice of Particle Flow*, China Construction Industry Press, Beijing, 2015.
- [24] B. K. Mishra and S. P. Mehrotra, "Modelling of particle stratification in jigs by the discrete element method," *Minerals Engineering*, vol. 11, no. 6, pp. 511–522, 1998.
- [25] X. Cai, Z. Zhou, H. Zang, and Z. Song, "Water saturation effects on dynamic behavior and microstructure damage of

- sandstone: phenomena and mechanisms,” *Engineering Geology*, vol. 276, article 105760, 2020.
- [26] C. Ma, Y. H. Tan, E. B. Li, and M. Yang, “Study on thermal conductivity of salt rock in the range of $-20^{\circ}\text{C} \sim 50^{\circ}\text{C}$,” *Journal of Rock Mechanics and Engineering*, vol. 31, no. S2, pp. 3725–3730, 2012.
- [27] X. Cai, Z. Zhou, L. Tan, H. Zang, and Z. Song, “Fracture behavior and damage mechanisms of sandstone subjected to wetting-drying cycles,” *Engineering Fracture Mechanics*, vol. 234, article 107109, 2020.
- [28] Z. W. Lou, *Damage Mechanics Foundation*, Xi’an Jiaotong University Press, Xi’an, 1991.
- [29] H. Y. Liu and G. W. Wang, “CHEN Fugang Research progress of rock damage theory characterized by damage variables,” *Blasting*, vol. 29, no. 1, pp. 9–12, 2004.
- [30] Z. W. Zhou, J. F. Liu, H. Zou, Y. Zhuo, and M. D. XuYang, “Acoustic emission characteristics and damage evolution of salt rock under uniaxial compression,” *Journal of Yangtze River Scientific Research Institute*, vol. 33, no. 5, pp. 63–68+75, 2016.
- [31] G. Xiang, J. F. Liu, T. Y. Li, M. D. XuYang, C. F. Deng, and C. Wu, “Research on fractal and damage characteristics of salt rock deformation and failure process based on acoustic emission,” *Rock and Soil Mechanics*, vol. 39, no. 8, pp. 2905–2912, 2018.
- [32] X. Cai, Z. Zhou, L. Tan, H. Zang, and Z. Song, “Water saturation effects on thermal infrared radiation features of rock materials during deformation and fracturing,” *Rock Mechanics and Rock Engineering*, vol. 53, no. 11, pp. 4839–4856, 2020.
- [33] L. Zhang and Y. Liu, “Damage evolution and acoustic emission characteristics analysis of coal rock based on particle discrete element model,” *Safety in Coal Mine*, vol. 48, no. 11, pp. 213–216, 2017.
- [34] M. D. Yao, *Experimental Study on Mechanical Properties and Crack Growth of Thermal Damaged Rock*, Wuhan University, Wuhan, 2017.
- [35] F. F. Meng, H. Pu, T. Sasaoka et al., “Time effect and prediction of broken rock bulking coefficient on the base of particle discrete element method,” *International Journal of Mining Science and Technology*, vol. 31, no. 4, pp. 643–651, 2021.
- [36] Z. J. Lu, H. M. Zhang, J. H. Chen, and M. Feng, “Shear strength and swelling pressure of unsaturated soil,” *Chinese Journal of Geotechnical Engineering*, vol. 14, no. 3, pp. 1–8, 1992.